

Nanoscale Origin of the Soft-to-Hard Short-Circuit Transition in Inorganic Solid-State Electrolytes

Chunyang Wang,^{*,†} Yubin He,[†] Peichao Zou, Qi He, Ju Li,^{*} and Huolin L. Xin^{*}



Cite This: <https://doi.org/10.1021/jacs.5c04113>



Read Online

ACCESS |



Metrics & More



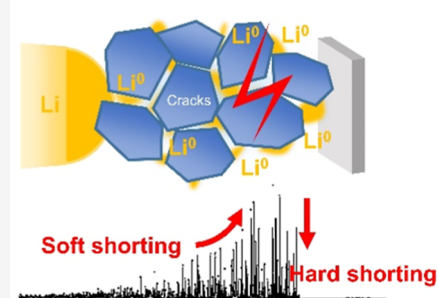
Article Recommendations



Supporting Information

ABSTRACT: Understanding and overcoming the chemomechanical failures of polycrystalline inorganic solid-state electrolytes (SSEs) are critical for next-generation all-solid-state batteries. Yet, so far, the nanoscale origin of SSEs' chemomechanical failure under operation conditions remains a mystery. Here, by using in situ electron microscopy, we decipher the nanoscale origin of the soft-to-hard short-circuit transition—a conventionally underestimated failure mechanism—caused by electronic leakage-induced Li^0 precipitation in SSEs. For the first time, we directly visualize stochastic Li^0 interconnection-induced soft short circuits, during which the SSEs undergo the transition from a nominal electronic insulator to a state exhibiting memristor-like nonlinear conduction (electronic leakages), ultimately evolving into hard short circuits. Furthermore, we first capture intragranular cracking caused by Li^0 penetration, demonstrating that fully wetted Li^0 can fracture polycrystalline oxide SSEs via a liquid-metal embrittlement-like mechanism. Guided by these insights, we show that incorporating an electronically insulating and mechanically resilient 3D polymer network into an inorganic/polymer composite SSE effectively suppresses Li^0 precipitation, interconnection, and short circuits, significantly enhancing its electrochemical stability. Our work, by elucidating the soft-to-hard short-circuit transition kinetics of SSEs, offers new insights into their nanoscale failure mechanisms.

Li^0 precipitation & interconnection



INTRODUCTION

All-solid-state batteries (ASSBs)^{1–5} have attracted considerable interest due to their improved safety compared to conventional lithium-ion batteries^{6,7} with flammable liquid electrolytes. As the key components of ASSBs, solid-state electrolytes (SSEs) play a crucial role in their performance and stability. So far, two types of SSEs, inorganic and polymeric SSEs, are mainly deployed in solid-state batteries. Inorganic SSEs including oxides^{8,9} and sulfides^{10,11} are highly promising for ASSBs due to their high ionic conductivity and elastic modulus. Yet, the chemomechanical instabilities of inorganic SSEs bring a grand challenge to their practical applications.¹² Polymer electrolytes are another SSE choice for ASSBs.^{13–18} However, due to their low elastic modulus, Li^0 morphological instabilities^{19,20} and displacive penetration through polymer electrolytes easily lead to short circuits and battery failure.²¹ In contradiction to the conventional view that dendrites can be inhibited by ceramic SSEs, which have a higher elastic modulus than Li metal, some recent studies^{12,22–24} propose that due to the minuscule (yet nonzero) electronic conductivity of inorganic SSEs (e.g., 1.2×10^{-8} S/cm in LATP²⁵ compared to its ionic conductivity of 6×10^{-4} S/cm),²⁶ electronic leakage-induced Li^0 precipitation in voids or at grain boundaries (GBs) can occur inside inorganic SSEs.²⁷ Here, we note that while most theoretical works idealized SSE as an electronic (e^-) insulator and ionic (Li^+) conductor in the linear-response regime, a large electric field (E) may trigger nonlinear responses, since a typical battery will sustain an average $E \sim V/\mu\text{m}$ across the SSE layer between the

cathode at ~ 4 V and the anode at 0 V, and the local E magnitude may easily be enhanced 10 \times by tip-curvature effects, i.e., in front of a metallic asperity. For comparison, a true wide-bandgap electronic insulator Al_2O_3 (alumina) only has a dielectric breakdown strength of 13.4 V/ μm .²⁸ Thus, it is conceivable that electronic leakage can occur in SSEs in real batteries, especially under local high-field conditions, near metallic asperities of the anode current collector (e.g., surface roughnesses from imperfect manufacturing). Charge-transfer (Faradaic) reactions can then occur at the following internal sites: $\text{Li}^0(\text{free volume}) = \text{Li}^+(\text{SSE}) + e^-(\text{SSE})$,²⁶ where $\text{Li}^0(\text{free volume})$ denotes a lithium adatom that is charge-neutral. These adatoms easily diffuse and aggregate into chains or clusters, and at some point, extended Li^0 precipitation and growth create a highway for electrons, consequently leading to short circuits. Also, such Li^0 precipitation is expected to lead to local stress concentration and mechanical fracture that further aggravate the degradation of inorganic SSEs. So far, although considerable efforts have been devoted to understanding the failure mechanism of inorganic SSEs,^{29–31} its nanoscale

Received: March 9, 2025

Revised: May 6, 2025

Accepted: May 7, 2025

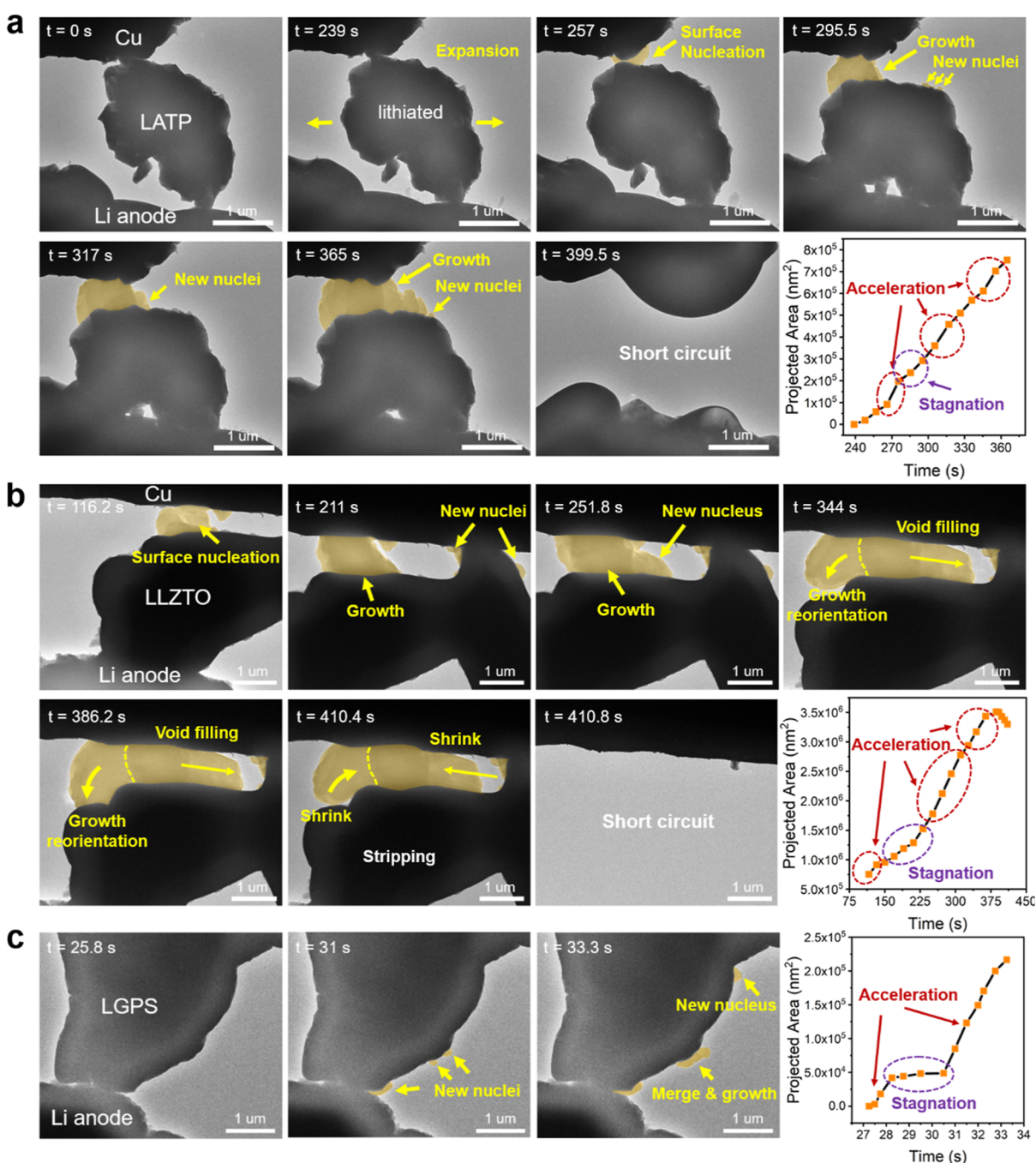


Figure 2. In situ observation of short-circuiting of inorganic SSEs induced by Li⁰ penetration/precipitation. (a) Time-resolved bright-field TEM (BF-TEM) images showing the in situ Li⁺ transportation and Li deposition with LAMP as the SSE. The projected area of Li⁰ was plotted as a function of time. (b) In situ Li⁺ transportation and Li deposition with garnet-type Li_{6.4}La₃Zr_{1.4}Ta_{0.6}O₁₂ (LLZTO) and the projected area of Li⁰ as a function of time. (c) In situ Li⁺ transportation and Li deposition with Li₁₀GeP₂S₁₂ (LGPS) and the projected area of Li⁰ as a function of time. The Li⁰ growth in all systems shows stochastic characteristics, that is, both stochastic acceleration and stagnation were observed during the Li deposition.

to LAMP-based Li–Li cells which fail rapidly (<100 h), Li–Li cells containing LAMP/polymer hybrid SSE demonstrate good stability (Figures S2–S4) and dramatically improved cycling performance (Figures 1c,e and S5) with a significantly lower overall impedance (Figure 1d). These results suggest that the polymer component not only suppresses electronic conduction but also facilitates ionic transport through the LAMP GBs.

High-resolution TEM (HRTEM) image and electron diffractions of pristine Li_{1.3}Al_{0.3}Ti_{1.7}(PO₄)₃ (LAMP) demonstrate that LAMP has a NASICON-type structure^{34,35} (see the

size distribution, atomic structure, and electronic conductivity of LAMP in Figures S6 and S7 and Table S1). Figure 2a and Movie S1 present time-resolved bright-field TEM images showing the in situ Li deposition process through the polycrystalline LAMP SSE. Upon lithiation by applying a voltage, the LAMP particle soon underwent a volume expansion ($t = 257$ s), after which metallic Li grew out from the particle surface and deposited onto the Cu electrode ($t = 295.5$ s). Aside from the growth of existing Li nuclei, Li⁰ was also observed to nucleate from other free-surface sites ($t = 365$

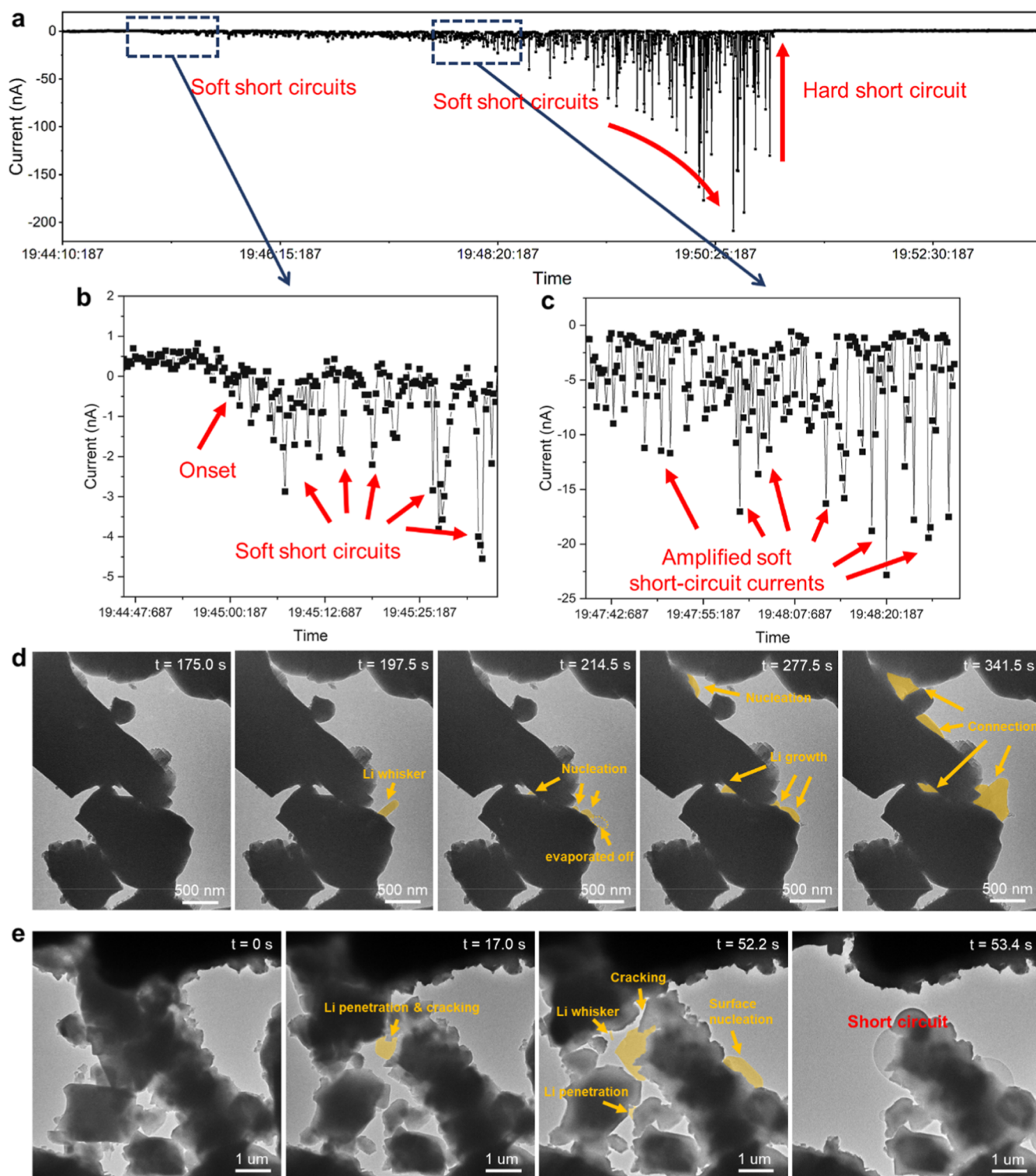


Figure 3. In situ observation of soft-to-hard short-circuit transition in inorganic SSEs. (a) Current as a function of time during the whole process of Li deposition with the LAMP system. (b,c) Zoomed-in current–time curves corresponding to the boxed regions in (a). The onset of soft short circuit is indicated in (b). High-frequency soft short circuits featured by intermittent current spikes (the amplitude of the spike increases with time) are indicated by arrows in (b,c). (d) Time-resolved BF-TEM images showing stochastic nucleation and growth of Li⁰ from multiple sites including free surface and internal voids. Subsequently, with the Li visibly linked together, the system short-circuited completely. (e) In situ observation of chemomechanical cracking induced by Li penetration at grain boundaries (GBs). The system finally short-circuited due to stochastic Li⁰ precipitation and interconnection.

s). Shortly after, the system short-circuited ($t = 399.5$ s), indicating that a highway for electrons, i.e., interconnected Li⁰, was formed across the entire SSE particle. To quantitatively

understand the Li⁰ evolution dynamics, the projected area of Li⁰ was plotted as a function of the deposition time (Figure 2a). We found that although the Li⁰ growth was nearly linear,

growth acceleration or stagnation occurred in certain periods. Detailed analysis (Figure S8) was performed on the lithiated LATP in the incipient stage before visible Li^0 precipitates at the particle surface. Electron energy-loss spectroscopy (EELS) of the Ti-L₂₃ edge (Figure S8c) shows that upon lithiation, the Ti valence shifts from Ti^{4+} toward lower energy (Ti^{3+}), suggesting a fully lithiated phase $\text{Li}_3\text{Al}_{0.3}\text{Ti}_{1.7}(\text{PO}_4)_3$ ³⁶ was formed due to a reduction reaction (see further discussion on how an SSE's reduction stability impacts Li penetration in Supporting Information). Yet, based on the area change (Figure S8a) between the pristine ($t = 0$ s) and lithiated phase ($t = 257$ s), the volume expansion was roughly estimated as $\sim 11\%$, evidently larger than the theoretical volume expansion ($\sim 6\%$) caused by the phase transformation (Figure S9). Although the possibility of crack formation in the particle cannot be ruled out, the nearly doubled volume expansion suggests that Li^+ was likely saturated in the LATP and Li^0 formed inside the particle. This is consistent with our observation that Li^0 subsequently penetrated the particle's surface and spilled over ($t = 257$ s, Figure 2a). Aside from LATP, other oxides and sulfide SSEs, including garnet-type $\text{Li}_{6.4}\text{La}_3\text{Zr}_{1.4}\text{Ta}_{0.6}\text{O}_{12}$ (LLZTO) and $\text{Li}_{10}\text{GeP}_2\text{S}_{12}$ (LGPS), were also explored. Figure 2b and Movie S2 present time-resolved bright-field TEM images showing the in situ dynamics of LLZTO during Li deposition. Upon lithiation, metallic Li grew out from the particle surface and a large Li^0 particle was formed in the "key hole" between the SSE and Cu electrode ($t = 116.2$ s). The Li^0 kept increasing in proportion through the coalescence of existing domains and the formation of new nuclei ($t = 251.8$ s). Interestingly, the Li^0 inclines to fill the "key hole" through lateral growth under compression (Li metal tends to diffusively creep like a Newtonian fluid when confined to less than $\sim 10^2$ nm at room temperature³⁷). With the hole almost filled, the left Li^0 grain gradually changed its growth direction ($t = 344$ s) from lateral to nearly vertical, leading to grain rotation ($t = 386.2$ s). Subsequently, with a reversed bias, although the grain rotation shows a reversible trend upon stripping, the cell short-circuited soon afterward ($t = 410.8$ s). The projected area of Li^0 plotted as a function of time shows that similar to that for LATP, the growth of Li^0 through LLZTO shows acceleration or stagnation at different stages. Similarly, we found that LGPS also suffered from Li^0 penetration, nonlinear Li^0 growth, and short circuit (Figure 2c). By estimating the amount of Li^0 plated from Figure 2 and applying Faraday's laws of electrolysis, we can estimate the Faradaic current from these dynamic microstructural observations. The magnitude of the Faradaic current is at most $\sim 10^2$ pA, which is below the noise floor of our ampere meter used in conjunction with the TEM holder. Note that a typical industrial-level current density in batteries is 3 mA/cm² (equivalent to a 3 mAh/cm² cathode under 1C charging). Given that the contact area under observation in Figure 2 is on the order of μm^2 , the corresponding Faradaic current in ASSBs is expected to be approximately 30 pA, indicating that our experiment closely approximates industrial conditions.

To investigate the underlying mechanism of the observed short-circuiting and breakdown of the inorganic SSEs, the total current flowing through the electrolyte was recorded in situ and correlated to their dynamic evolutions. Figure 3a shows the current curve flowing through the LATP SSE recorded over its whole life. It is found that during the in situ deposition process, the current kept building up until the whole system suddenly short-circuited and burnt out (Figure 3a). Figure 3b

shows the zoomed-in current curve corresponding to the left-side boxed region in Figure 3a. We found that the current at the beginning is low (equivalent to the background noise of ~ 0.5 nA). At a certain point, the current abruptly increased, followed by high-frequency stochastic spikes that indicate transient short circuit and meltdowns within the electrolyte. The observed electronic-conduction dynamics closely mirror those characteristic of dielectric breakdown and memristor-type switching. The nA-level current corresponds to electronic current rather than ionic current, as nothing about ionic conduction can reach this magnitude ($\sim 10^2$ pA level and not measurable in our case as it is beyond the detection limit), nor could it vary so violently with time. Thus, by quantitative microstructural evolution and amperometry, we can separate out the Faradaic and non-Faradaic electronic currents. The non-Faradaic electronic bursts are much larger in amplitude and shorter in duration, similar to those in nanoscale dielectric breakdowns of insulators like Al_2O_3 and HfO_2 under high field. They can kick-start the autocatalytic Faradaic reaction $\text{Li}^0(\text{free volume}) = \text{Li}^+(\text{SSE}) + \text{e}^-(\text{SSE})$, where more bridging $\text{Li}^0(\text{free volume})$ can form atomic filaments²⁶ that increase the availabilities of $\text{e}^-(\text{SSE})$ and E_{up} . With prolonged operation, although the frequency of the soft short circuit remains almost unchanged, the amplitude of the current spike gradually increased to hundreds of nA (Figure 3c). At a certain point, the current suddenly dropped to nearly zero, indicating that the system completely short-circuited and then disintegrated by melting like a fuse. Figure 3d and Movie S3 show time-resolved bright-field TEM images of a bunch of interconnected LATP particles (current flowing through the LATP is shown in Figure 3a) during in situ Li^0 deposition. Upon lithiation, a Li whisker soon nucleated and grew out from the particle surface ($t = 197.5$ s). Subsequently, the whisker melted or evaporated off under increased current due to the short circuit, yet new Li^0 domains nucleated stochastically from free surfaces and voids/gaps between the LATP particles ($t = 214.5$ s); during this period, although the whole electrolyte was not visibly covered by Li^0 , a highway for electrons was already created transiently (indicated by stochastic current spikes as shown in Figure 3a–c). In the following stage, the Li^0 domains kept growing rapidly ($t = 277.5$ s) and, ultimately, the whole system completely short-circuited (Figure S10) when the Li^0 domains became visibly interconnected with each other ($t = 341.5$ s). From the above, the short circuit followed by a short period of recovery suggests that the electron highway can be transiently broken up by meltdown or evaporation of local Li_0 domains, which is essentially a form of soft short circuit and could be responsible for the growth stagnation observed in Figure 2. Figure 3e and Movie S4 show another case whereby chemomechanical failure caused by Li^0 penetration at GBs was directly observed. We found that upon lithiation, the whole electrolyte broke into pieces with metallic Li spilling over from the GBs ($t = 17$ s); meanwhile, grain rotation caused by large internal stress between the LATP grains was also observed (in regions on the left side). This final stage of damage reminds one of the liquid-metal embrittlement in metallurgy³³ where reactive wetting of steel/Al GBs by liquid Na/Ga causes the granular assembly to completely disintegrate, except here, the matrix grains are an oxide instead of a metal. With further growth of the Li^0 between the grains, the cracking of the oxide electrolyte was exacerbated, and, in the meantime, Li^0 domains and whiskers burst from the free surfaces ($t = 52.2$ s). Similar to the case in Figure 3d, the stochastic Li^0 precipitation and interconnection

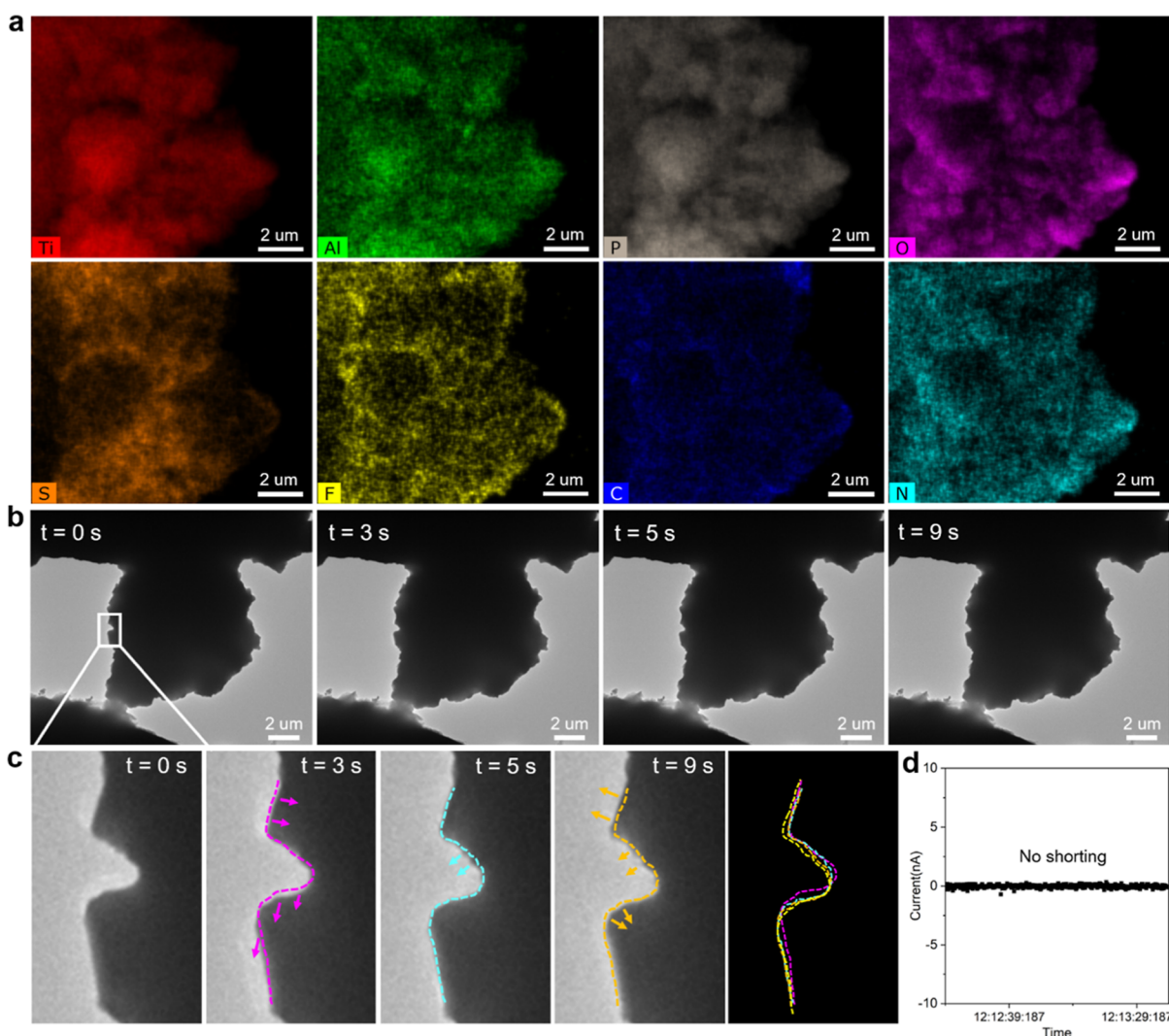


Figure 4. Chemomechanically stable Li^+ transportation in a LATP/polymer hybrid SSE. (a) Energy-dispersive spectroscopy (EDS) maps of the LATP/polymer hybrid SSE. (b) Time-resolved BF-TEM images of the LATP/polymer hybrid SSE upon in situ lithiation. (c) Enlarged images corresponding to the boxed region in (b). The dashed line highlights the surface profile of the SSE particle in the previous frame. The wavy movement of the surface indicates coordinative deformation between the flexible polymer network and the inorganic SSE particles upon lithiation. (d) Current as a function of time during the whole process of Li deposition with LATP/polymer hybrid SSE. The current remains stable as a function of time (close to the background noise).

finally resulted in a complete short circuit of the system ($t = 53.4$ s). In short, an initial nonlinear electronic “vicious cycle” triggered the onset of SSE degradation, which gradually evolved into a nonlinear mechanical “vicious cycle”.

To mitigate the soft-to-hard short-circuit transition and its resultant chemomechanical breakdowns and disintegration of inorganic SSEs, a mechanically flexible 3D polymer network (EA-LiFSI-EIMFSI-FEC; see synthesis details in [Supporting Information](#)) was introduced to form an LATP/polymer hybrid SSE (the polymer was mixed with the LATP powder with a mass ratio of 1:2; see details in [Supporting Information](#)). [Figure 4a](#) shows the elemental maps of the LATP/polymer hybrid SSE. It is seen that the polycrystalline LATP particles and the polymer network form a well-blended nanocomposite. That is, the rigid LATP crystals are well wrapped around by the polymer network. In situ Li deposition experiment shows that the LATP/polymer hybrid SSE remained stable during the lithiation process ([Figure 4b](#) and [Movie S5](#); also see the full-length video in [Movie S6](#) and the

corresponding current–time curve in [Figure S11](#)). [Figure 4c](#) shows enlarged images corresponding to the boxed region in [Figure 4b](#). The dashed line highlights the surface profile of the solid electrolyte in the previous frame. Different from the pure LATP, which undergoes rigid expansion at all sites during lithiation and easily cracks, the LATP/polymer hybrid SSE undergoes coordinative deformation between the flexible polymer network (acting as a mechanically resilient buffering layer) and the inorganic solid electrolyte particles featured by the wavy movement of the electrolyte’s surface as shown in [Figure 4c](#) and [Movie S7](#). The robust mechanical stability of the LATP/polymer hybrid SSE was also validated by in situ deformation experiments in TEM. In stark contrast to the pure LATP system easily cracking during deformation ([Figure S12](#)), the hybrid electrolyte remains almost intact after reversible deformation up to over 200 cycles ([Figure S13](#)). In addition, distinct from pure inorganic SSEs, which suffer from high-frequency soft short circuit events featuring $> \text{nA}$ non-Faradaic spikes on the current–time curve, the current flowing through

the LATP/polymer hybrid SSE remains below the noise floor of our TEM holder's ampere meter (Figure 4d) as it should be, indicating that soft short circuits were effectively suppressed even under the same operation conditions.

DISCUSSION

The failure of SSEs has often been attributed to chemical and electrochemical instabilities at the SSE/Li interface, where interfacial side reactions compromise the electrolyte's integrity.^{38,39} While we acknowledge that such side reactions play an important role in battery degradation, our findings emphasize the importance of another key failure mechanism—Li penetration and the resultant soft-to-hard short-circuit transition. Through operando TEM, we first experimentally confirmed that transient soft short circuit events, driven by Li infiltration along GBs or voids, can gradually evolve into a percolating electron pathway, ultimately leading to catastrophic hard short circuits. This process suggests that while interfacial degradation may contribute to the instability of SSEs, the Li-metal-penetration-induced mechanical disintegration and short circuit are crucial and often underappreciated factors in battery failure. Our in situ TEM experiments highlight that even in the absence of severe interfacial degradation, Li penetration alone can initiate a self-reinforcing cycle of electronic leakage and structural breakdown. Thus, to develop more robust SSEs, strategies aimed at mitigating Li penetration—such as interfacial engineering or mechanical reinforcement—should be considered alongside efforts to improve interfacial stability.

The nanoscale interrogation of the structure–performance relationship of SSEs in this work fundamentally confirms that integrating inorganic electrolytes with dynamic polymer networks is a crucial strategy for developing high-performance SSEs.^{38–40} Our results show that the polymer network offers three key advantages. First, it introduces an electronically more insulating (the polymeric SSE's electronic conductivity is measured to be $\sim 1.09 \times 10^{-10}$ S/cm (Figure S14), 2 orders of magnitude lower than that of LATP²⁵) but ionically conducting interface between neighboring grains. Considering the charge–transfer reaction $\text{Li}^0(\text{free volume}) = \text{Li}^+(\text{SSE}) + \text{e}^-(\text{SSE})$: with $\text{e}^-(\text{SSE})$ much more difficult to come by, and with $\text{Li}^+(\text{SSE})$ passing rapidly across the inorganic GB via the polymer bridge, there is less chance for $\text{Li}^+(\text{SSE})$ to dwell near the GB, meet an electron, and become reduced into the $\text{Li}^0(\text{free volume})$ adatom. We note that our solid polymer electrolyte (SPE) is a better electronic insulator than the oxide SSEs not only in the linear sense but likely in the nonlinear sense. Second, despite its lower elastic modulus, the polymer chains can sustain some tensile stress, while ceramic GBs can hardly sustain any. The polymer network acts as a mechanically resilient buffer that could effectively accommodate the plastic strain generated by the inorganic particle's volume change. This enables the nanocomposite SSE to impart compressive stress onto ceramic grains, suppressing crack propagation and enhancing mechanical stability. Third, the strong adhesion and intimate binding of the SPE, which acts as an organic binder between ceramic grains, reduce the driving force for GB wetting by Li^0 and “liquid-metal embrittlement” tendencies. Yet, it should be noted that, for the design of composite/hybrid SSEs, it is important to consider not only the chemical/electrochemical compatibility between inorganic SSEs and Li metal (see a detailed discussion and Figure S15 in the Supporting Information) but also their compatibility with polymer chemistry.

CONCLUSIONS

In summary, we elucidate the nanoscale origin of the soft-to-hard short-circuit transition in inorganic SSEs through in situ electron microscopy with high spatial and temporal resolution. Our findings reveal that soft short circuits—characterized by dynamically reversible non-Faradaic electronic breakdowns—originate from transient interconnections and localized melting of precipitated Li^0 at the nanoscale, which ultimately evolve into hard short circuits marked by amplified electronic leakage. This failure mechanism is universally observed in both NASICON- and garnet-type inorganic SSEs. By integrating a flexible polymer network into rigid inorganic SSEs to mitigate electronic leakage while preserving ionic transport, we demonstrate a significant enhancement in electrolyte stability and cycling performance. This new mechanistic insight and proof-of-concept strategy offer a broadly applicable framework for designing next-generation SSEs for high-energy-density, long-life ASSBs.

ASSOCIATED CONTENT

Supporting Information

The Supporting Information is available free of charge at <https://pubs.acs.org/doi/10.1021/jacs.5c04113>.

Materials and electrochemical tests; details of in situ TEM experiments; and additional electrochemical, SEM, TEM characterizations of the solid-state electrolytes (PDF)

Time-resolved bright-field TEM images showing the in situ Li deposition process through the polycrystalline LATP SSE (AVI)

Time-resolved bright-field TEM images showing the in situ dynamics of LLZTO during Li deposition (AVI)

Time-resolved bright-field TEM images of a bunch of interconnected LATP particles (AVI)

Chemomechanical failure caused by Li^0 penetration at grain boundaries (AVI)

In situ Li deposition experiment showing that the LATP/polymer hybrid SSE remained stable during the lithiation process (AVI)

In situ Li deposition experiment shows that the LATP/polymer hybrid SSE remained stable during the lithiation process (AVI)

LATP/polymer hybrid SSE undergoing coordinative deformation between the flexible polymer network (acting as a mechanically resilient buffering layer) and the inorganic solid electrolyte particles featured by the wavy movement of the electrolyte's surface (AVI)

AUTHOR INFORMATION

Corresponding Authors

Chunyang Wang – Department of Physics and Astronomy, University of California Irvine, Irvine, California 92697, United States; Shenyang National Laboratory for Materials Science, Institute of Metal Research, Chinese Academy of Sciences, Shenyang 110016, China; orcid.org/0000-0001-8461-3952; Email: wangchunyang@imr.ac.cn

Ju Li – Department of Nuclear Science and Engineering, Massachusetts Institute of Technology, Cambridge, Massachusetts 02139, United States; Department of Materials Science and Engineering, Massachusetts Institute of Technology, Cambridge, Massachusetts 02139, United States

States; orcid.org/0000-0002-7841-8058; Email: liju@mit.edu

Huolin L. Xin – Department of Physics and Astronomy, University of California Irvine, Irvine, California 92697, United States; orcid.org/0000-0002-6521-868X; Email: huolin.xin@uci.edu

Authors

Yubin He – Department of Physics and Astronomy, University of California Irvine, Irvine, California 92697, United States; orcid.org/0000-0002-3434-4595

Peichao Zou – Department of Physics and Astronomy, University of California Irvine, Irvine, California 92697, United States

Qi He – Department of Nuclear Science and Engineering, Massachusetts Institute of Technology, Cambridge, Massachusetts 02139, United States

Complete contact information is available at:

<https://pubs.acs.org/10.1021/jacs.Sc04113>

Author Contributions

[†]C.W. and Y.H. contributed equally.

Notes

The authors declare no competing financial interest.

ACKNOWLEDGMENTS

This work is supported by the Materials Science and Engineering Divisions, Office of Basic Energy Sciences of the U.S. Department of Energy, under award no. DE-SC0021204. J.L. acknowledges support by NSF CBET-2034902. This research used the resources of the Center for Functional Nanomaterials (CFN), which is a U.S. Department of Energy Office of Science User Facility, at Brookhaven National Laboratory under Contract No. DE-SC0012704. Part of the write-up was completed after C.W. left UC Irvine.

REFERENCES

- (1) Liu, X.; Garcia-Mendez, R.; Lupini, A. R.; Cheng, Y.; Hood, Z. D.; Han, F.; Sharafi, A.; Idrobo, J. C.; Dudney, N. J.; Wang, C.; Ma, C.; Sakamoto, J.; Chi, M. Local electronic structure variation resulting in Li 'filament' formation within solid electrolytes. *Nat. Mater.* **2021**, *20*, 1485–1490.
- (2) Jin, Y.; Liu, K.; Lang, J.; Zhuo, D.; Huang, Z.; Wang, C.-a.; Wu, H.; Cui, Y. An intermediate temperature garnet-type solid electrolyte-based molten lithium battery for grid energy storage. *Nat. Energy* **2018**, *3* (9), 732–738.
- (3) Kasemchainan, J.; Zekoll, S.; Spencer Jolly, D.; Ning, Z.; Hartley, G. O.; Marrow, J.; Bruce, P. G. Critical stripping current leads to dendrite formation on plating in lithium anode solid electrolyte cells. *Nat. Mater.* **2019**, *18* (10), 1105–1111.
- (4) Ning, Z.; Jolly, D. S.; Li, G.; De Meyere, R.; Pu, S. D.; Chen, Y.; Kasemchainan, J.; Ihli, J.; Gong, C.; Liu, B.; Melvin, D. L. R.; Bonnin, A.; Magdysyuk, O.; Adamson, P.; Hartley, G. O.; Monroe, C. W.; Marrow, T. J.; Bruce, P. G. Visualizing plating-induced cracking in lithium-anode solid-electrolyte cells. *Nat. Mater.* **2021**, *20*, 1121–1129.
- (5) Balaish, M.; Gonzalez-Rosillo, J. C.; Kim, K. J.; Zhu, Y.; Hood, Z. D.; Rupp, J. L. M. Processing thin but robust electrolytes for solid-state batteries. *Nat. Energy* **2021**, *6* (3), 227–239.
- (6) Suo, L.; Borodin, O.; Gao, T.; Olguin, M.; Ho, J.; Fan, X.; Luo, C.; Wang, C.; Xu, K. Water-in-salt[†] electrolyte enables high-voltage aqueous lithium-ion chemistries. *Science* **2015**, *350* (6263), 938–943.
- (7) von Wald Cresce, A.; Xu, K. Aqueous lithium-ion batteries. *Carbon Energy* **2021**, *3* (5), 721–751.

- (8) Paoletta, A.; Liu, X.; Daali, A.; Xu, W.; Hwang, I.; Savoie, S.; Girard, G.; Nita, A. G.; Perea, A.; Demers, H.; Zhu, W.; Guerfi, A.; Vijh, A.; Bertoni, G.; Gazzadi, G. C.; Berti, G.; Sun, C.; Ren, Y.; Zaghbi, K.; Armand, M.; Kim, C.; Xu, G. L.; Amine, K. Enabling High-Performance NASICON-Based Solid-State Lithium Metal Batteries Towards Practical Conditions. *Adv. Funct. Mater.* **2021**, *31* (30), 2102765.

- (9) Zhai, W.; Zhang, Y.; Shi, H.; Hu, X.; Hao, R.; Liu, W.; Yu, Y. Quantifying the Growth Kinetics of Lithium Metal Reduced from Solid Ionic Conductors. *J. Am. Chem. Soc.* **2024**, *146* (20), 14095–14104.

- (10) Wu, J.; Liu, S.; Han, F.; Yao, X.; Wang, C. Lithium/Sulfide All-Solid-State Batteries using Sulfide Electrolytes. *Adv. Mater.* **2021**, *33* (6), 2000751.

- (11) Xu, R.; Yue, J.; Liu, S.; Tu, J.; Han, F.; Liu, P.; Wang, C. Cathode-Supported All-Solid-State Lithium–Sulfur Batteries with High Cell-Level Energy Density. *ACS Energy Lett.* **2019**, *4* (5), 1073–1079.

- (12) Liu, H.; Cheng, X.-B.; Huang, J.-Q.; Yuan, H.; Lu, Y.; Yan, C.; Zhu, G.-L.; Xu, R.; Zhao, C.-Z.; Hou, L.-P.; He, C.; Kaskel, S.; Zhang, Q. Controlling Dendrite Growth in Solid-State Electrolytes. *ACS Energy Lett.* **2020**, *5* (3), 833–843.

- (13) Yue, L.; Ma, J.; Zhang, J.; Zhao, J.; Dong, S.; Liu, Z.; Cui, G.; Chen, L. All solid-state polymer electrolytes for high-performance lithium ion batteries. *Energy Storage Mater.* **2016**, *5*, 139–164.

- (14) Dong, T.; Zhang, J.; Xu, G.; Chai, J.; Du, H.; Wang, L.; Wen, H.; Zang, X.; Du, A.; Jia, Q.; Zhou, X.; Cui, G. A multifunctional polymer electrolyte enables ultra-long cycle-life in a high-voltage lithium metal battery. *Energy Environ. Sci.* **2018**, *11* (5), 1197–1203.

- (15) Wu, J.; Rao, Z.; Cheng, Z.; Yuan, L.; Li, Z.; Huang, Y. Ultrathin, Flexible Polymer Electrolyte for Cost-Effective Fabrication of All-Solid-State Lithium Metal Batteries. *Adv. Energy Mater.* **2019**, *9* (46), 1902767.

- (16) Lu, Q.; He, Y. B.; Yu, Q.; Li, B.; Kaneti, Y. V.; Yao, Y.; Kang, F.; Yang, Q. H. Dendrite-Free, High-Rate, Long-Life Lithium Metal Batteries with a 3D Cross-Linked Network Polymer Electrolyte. *Adv. Mater.* **2017**, *29* (13), 1604460.

- (17) Qiu, J.; Liu, X.; Chen, R.; Li, Q.; Wang, Y.; Chen, P.; Gan, L.; Lee, S. J.; Nordlund, D.; Liu, Y.; Yu, X.; Bai, X.; Li, H.; Chen, L. Enabling Stable Cycling of 4.2 V High-Voltage All-Solid-State Batteries with PEO-Based Solid Electrolyte. *Adv. Funct. Mater.* **2020**, *30* (22), 1909392.

- (18) Nie, K.; Wang, X.; Qiu, J.; Wang, Y.; Yang, Q.; Xu, J.; Yu, X.; Li, H.; Huang, X.; Chen, L. Increasing Poly(ethylene oxide) Stability to 4.5 V by Surface Coating of the Cathode. *ACS Energy Lett.* **2020**, *5* (3), 826–832.

- (19) Wang, C.; Lin, R.; He, Y.; Zou, P.; Kisslinger, K.; He, Q.; Li, J.; Xin, H. L. Tension-Induced Cavitation in Li-Metal Stripping. *Adv. Mater.* **2023**, *35* (7), 2209091.

- (20) Wang, C.; Wang, H.; Tao, L.; Wang, X.; Cao, P.; Lin, F.; Xin, H. L. Direct Observation of Nucleation and Growth Behaviors of Lithium by In Situ Electron Microscopy. *ACS Energy Lett.* **2023**, *8* (4), 1929–1935.

- (21) Rosso, M.; Brissot, C.; Teyssot, A.; Dollé, M.; Sannier, L.; Tarascon, J.-M.; Bouchet, R.; Lascaud, S. Dendrite short-circuit and fuse effect on Li/polymer/Li cells. *Electrochim. Acta* **2006**, *51* (25), 5334–5340.

- (22) Kazyak, E.; Garcia-Mendez, R.; LePage, W. S.; Sharafi, A.; Davis, A. L.; Sanchez, A. J.; Chen, K.-H.; Haslam, C.; Sakamoto, J.; Dasgupta, N. P. Li Penetration in Ceramic Solid Electrolytes: Operando Microscopy Analysis of Morphology, Propagation, and Reversibility. *Matter* **2020**, *2* (4), 1025–1048.

- (23) Wang, M. J.; Kazyak, E.; Dasgupta, N. P.; Sakamoto, J. Transitioning solid-state batteries from lab to market: Linking electrochemo-mechanics with practical considerations. *Joule* **2021**, *5* (6), 1371–1390.

- (24) Han, F.; Yue, J.; Zhu, X.; Wang, C. Suppressing Li Dendrite Formation in Li2S-P2S5 Solid Electrolyte by LiI Incorporation. *Adv. Energy Mater.* **2018**, *8* (18), 1703644.

- (25) Zhao, E.; Ma, F.; Jin, Y.; Kanamura, K. Pechini synthesis of high ionic conductivity $\text{Li}_{1.3}\text{Al}_{0.3}\text{Ti}_{1.7}(\text{PO}_4)_3$ solid electrolytes: The effect of dispersant. *J. Alloys Compd.* **2016**, *680*, 646–653.
- (26) Dong, Y.; Chen, I.-W.; Li, J. Transverse and Longitudinal Degradations in Ceramic Solid Electrolytes. *Chem. Mater.* **2022**, *34* (13), 5749–5765.
- (27) Han, F.; Westover, A. S.; Yue, J.; Fan, X.; Wang, F.; Chi, M.; Leonard, D. N.; Dudney, N. J.; Wang, H.; Wang, C. High electronic conductivity as the origin of lithium dendrite formation within solid electrolytes. *Nat. Energy* **2019**, *4* (3), 187–196.
- (28) Haynes, W. M.; Lide, D. R.; Bruno, T. J. *CRC Handbook of Chemistry and Physics*; CRC Press, 2016.
- (29) Gu, J.; Chen, X.; He, Z.; Liang, Z.; Lin, Y.; Shi, J.; Yang, Y. Decoding Internal Stress-Induced Micro-Short Circuit Events in Sulfide-Based All-Solid-State Li-Metal Batteries via Operando Pressure Measurements. *Adv. Energy Mater.* **2023**, *13* (47), 2302643.
- (30) Wang, C.; Deng, T.; Fan, X.; Zheng, M.; Yu, R.; Lu, Q.; Duan, H.; Huang, H.; Wang, C.; Sun, X. Identifying soft breakdown in all-solid-state lithium battery. *Joule* **2022**, *6* (8), 1770–1781.
- (31) Menkin, S.; Fritzsche, J. B.; Larner, R.; de Leeuw, C.; Choi, Y.; Gunnarsdóttir, A. B.; Grey, C. P. Insights into Soft Short Circuit-based Degradation of Lithium Metal Batteries. *Faraday Discuss.* **2024**, *248*, 277–297.
- (32) Kim, S. Y.; Li, J. Porous Mixed Ionic Electronic Conductor Interlayers for Solid-State Batteries. *Adv. Energy Mater.* **2021**, *2021*, 1–15.
- (33) Nicholas, M.; Old, C. Liquid metal embrittlement. *J. Mater. Sci.* **1979**, *14* (1), 1–18.
- (34) Goodenough, J. B. NASICON I Structure and conductivity. *Solid State Ionics* **1983**, *9*, 793–794.
- (35) Aono, H.; Sugimoto, E.; Sadaoka, Y.; Imanaka, N.; Adachi, G. y. Ionic Conductivity of the Lithium Titanium Phosphate ($\text{Li}_1 + \text{X M X Ti}_2 - \text{X}(\text{PO}_4)_3$, $\text{M} = \text{Al, Sc, Y, and La}$) Systems. *J. Electrochem. Soc.* **1989**, *136* (2), 590–591.
- (36) Zhu, J.; Zhao, J.; Xiang, Y.; Lin, M.; Wang, H.; Zheng, B.; He, H.; Wu, Q.; Huang, J. Y.; Yang, Y. Chemomechanical Failure Mechanism Study in NASICON-Type $\text{Li}_{1.3}\text{Al}_{0.3}\text{Ti}_{1.7}(\text{PO}_4)_3$ Solid-State Lithium Batteries. *Chem. Mater.* **2020**, *32* (12), 4998–5008.
- (37) Chen, Y.; Wang, Z.; Li, X.; Yao, X.; Wang, C.; Li, Y.; Xue, W.; Yu, D.; Kim, S. Y.; Yang, F.; Kushima, A.; Zhang, G.; Huang, H.; Wu, N.; Mai, Y.-W.; Goodenough, J. B.; Li, J. Li metal deposition and stripping in a solid-state battery via Coble creep. *Nature* **2020**, *578* (7794), 251–255.
- (38) He, Y.; Wang, C.; Zhang, R.; Zou, P.; Chen, Z.; Bak, S. M.; Trask, S. E.; Du, Y.; Lin, R.; Hu, E.; Xin, H. L. A self-healing plastic ceramic electrolyte by an aprotic dynamic polymer network for lithium metal batteries. *Nat. Commun.* **2024**, *15* (1), 10015.
- (39) He, Y.; Wang, C.; Lin, R.; Hu, E.; Trask, S. E.; Li, J.; Xin, H. L. A Self-Healing, Flowable, Yet Solid Electrolyte Suppresses Li-Metal Morphological Instabilities. *Adv. Mater.* **2024**, *36* (49), 2406315.
- (40) Liu, S.; Liu, W.; Ba, D.; Zhao, Y.; Ye, Y.; Li, Y.; Liu, J. Filler-Integrated Composite Polymer Electrolyte for Solid-State Lithium Batteries. *Adv. Mater.* **2023**, *35* (2), 2110423.